CORROSION PROTECTION AND CHARACTERIZATION OF TRIMETAL OXIDES NANOCOMPOSITE COATED METAL SUBSTRATES PREPARED BY RADIO FREQUENCY SPUTTERING DEPOSITION

A Thesis

by

MINHO LEE

Submitted to the Office of Graduate and Professional Studies of
Texas A&M University
in partial fulfillment of the requirements for the degree of

MASTER OF SCIENCE

Chair of Committee,	Homero Castaneda-Lopez
Co-Chair of Committee,	Raymundo Case
Committee Member,	Sreeram Vaddiraju
Head of Department,	Ibrahim Karaman

August 2020

Major Subject: Materials Science and Engineering

ABSTRACT

Titanium oxide (TiO_2) represents the self-cleaning feature with a combination of photo-catalysis and photo-induced super-hydrophilicity. However, TiO_2-coated carbon steel (CS) and stainless steel (SS) have not presented the corrosion protection ability and nanostructured coating stability. In the present work, we have synthesized the novel tri-metallic oxide nanocomposites based on zirconium oxide (ZrO_2), zinc oxide (ZnO), and TiO_2 by varying the different compositions from mechano-chemical process to improve the corrosion protection and coating stability of ZrO_2/ZnO/TiO_2 nanocomposites on CS and SS surfaces. Metallization was observed to the phase identification of powder samples examined by X-ray diffraction (XRD) with an average crystallite size less than 20 nm. SEM images showed distinct distribution of grains with the formation of agglomeration. The coating was made on CS and SS with a target prepared from four different compositions having a thickness around 50 nm via radio frequency sputtering to investigate the performance of coatings studied by electrochemical impedance spectroscopy (EIS). The samples were exposed to 3.5% NaCl solution for 10 days at room temperature.

From the Bode plots, the impedance of ZrO_2-rich composition coated CS and SS samples exhibited higher values about 3 - 4 times of magnitude than those of bare CS and SS samples at the low frequency region after 10 day immersion. Interestingly enough, the phase angle values of ZrO_2-rich composition coated CS and SS samples showed around -48° and -82°, respectively, with decreasing frequency. This is because relatively denser pore surface of coating materials was performed by the uniform distribution morphologies

of ZrO_2/ZnO/TiO_2 nanocomposites, which makes it more difficult for NaCl solution to penetrate into coating layer on CS and SS substrates. ZrO_2 seems to inhibit the corrosion more strongly on the interface between NaCl solution and coating layers. ZrO_2 would facilitate good corrosion protection of CS and SS coated by ZrO_2/ZnO/TiO_2 nanocomposites.

ACKNOWLEDGEMENTS

I would like to thank my committee chair, Dr. Castaneda, Homero, and my committee members, Dr. Case, Raymundo, Dr. Vaddiraju, Sreeram, and Prof. Subramaniam, Velumani and Prof. Kim, Jeongho, for their guidance and support throughout the course of this research.

Thanks also go to my friends and colleagues and the department faculty and staff for making my time at Texas A&M University a great experience.

Finally, thanks to my family for their encouragement.

CONTRIBUTORS AND FUNDING SOURCES

Contributors

This work was supervised by a thesis committee consisting of Professor Castaneda, Homero and Professor Case, Raymundo of the Department of Materials Science and Engineering.

The data analyzed for Chapter 3 was provided by Professor Subramaniam, Velumani. The analyses depicted in Chapter 4 were conducted in part by Professor Subramaniam, Velumani of the Department of Electrical Engineering at CINVESTAV in Mexico.

TABLE OF CONTENTS

Page

LIST OF FIGURES

Page

LIST OF TABLES

Page

1. INTRODUCTION

Nanotechnology has emerged as a steppingstone skill interdisciplinary with physics, chemistry, biology, medicine, and material science dealing with the materials of diverse types at a nanoscale level [1]. A broad terminology of nanotechnology was presented by Nobel laureate Richard P. Feynman in his famous lecture given at the American physical society meeting held in 1959 [2]. Distinctive definition of nanoparticles (NPs) can be explained from three Cartesian dimensions having less than 100 nm with a surrounding interfacial layer. NPs are composed of three different interfacial layers namely, surface layer, shell layer, and the core therefore, the extent of interest can be seen in researchers as multidisciplinary fields. These dimensions are larger than the size of individual atoms or molecules but smaller than bulk solids [3]. NPs can be categorized into zero-dimensional (0D), one dimensional (1D), two dimensional (2D) or three dimensional (3D) depending on the overall shape of these materials [3, 4]. However, the physical and chemical properties of nanoparticles and bulk materials are different. Nanoclusters and soft bio-organic nanoparticles are also synonyms of NPs. A dimensional explanation of nanocluster is the combination of the equally sized nanoparticles having nanometer dimensions. A crucial demonstration can be shown by NPs and nano-metal clusters in the state of condensed matter. Although, NPs illustrate a divergence between the atomic or molecular structure and bulk materials [5].

A beauty of these materials realized when investigators found that these nano-scopic sizes can influence acutely the physiochemical properties of the substance by the fact on the study of NPs based on gold (Au), platinum (Pt), silver (Ag), and palladium (Pd)

with the characteristics of wine red, yellowish gray, black and dark black colors, respectively [6]. The difference in the colors of these materials is due to the fluctuation of absorption properties at the nanoscale level. NPs are largely partitioned into various categories by the consideration of structural, morphological, particle size and surface area, optical, chemical characterizations. Carbon-based NPs, ceramics-NPs, semiconductor-NPs, polymer-NPs, lipid-based NPs, and metal-based NPs are functionalized well known NPs based on physical and chemical properties [4, 7].

Carbon nanotubes (CNTs) and fullerenes are two major classes that represent the carbon-based NPs [8]. Structurally, CNTs are elongated and tubular having 1-2 nm in diameter which can be predicted as metallic or semiconducting behavior with the resemblance of single-walled to multi-walled self-rolling graphite sheets. Fullerenes nanomaterials are a globular hollow cage in structure with a diameter of around 7 nm holding their unique characteristics such as electrical conductivity, high strength, electron affinity, and flexibility [9]. Solid inorganic nano-metals have belonged to ceramic NPs which can be found in amorphous, polycrystalline, porous or hollow form synthesized employing heat and successive cooling in conjunction with their versatility in catalysis, photo-catalysis, imaging and photo-degradation applications [8-10]. Tunable bandgap nanomaterials possessing properties between metals and insulators have their place to semiconductor NPs owing to its elevated usefulness in photo-catalysis, photo optics, and electronic devices. Polymeric NPs are organic with the dominant structure of nano-spheres or nanocapsules [11]. Nano-spheres are matrix particles having the solid entire mass where absorption of molecules takes place at the spherical surface. However, solid mass is encapsulated within the particle completely in the latter case. Lipid-based NPs are

characteristically spherical with the diameter ranging from 10 to 100 nm applicable in biomedical purposes effectively [12]. It acquires a solid core made of lipid and a matrix comprises soluble lipophilic molecules. Metal NPs are solely made of the metal precursors acquiring unique optoelectrical properties due to well-known localized surface Plasmon resonance [13]. NPs of alkali and noble metals have a broad absorption band in the visible spectrum obeying huge viable potential in the various applications from research and development to environmental purposes.

1.1. Multi-metallic nanocomposites

The last couple of decades have observed a surge in the use of multi-metallic nanocomposite materials due to their remarkable properties in comparison to their bulk counterparts [14]. Monometallic nanoparticles (MNPs) consist of only particular metal and are of different types reliant on the type of metal atom present such as magnetic, metallic and transition metal nanoparticles, etc [15]. The structure of MNPs can be stabilized via different functional groups. Bimetallic nanoparticles (BNPs) are composed of two different metals and immense attention has been drawn then the MNPs from both scientific as well as technological realm [16]. The catalytic properties of the nanoparticles can be enhanced to a great extent after the bi-metallization in the form of alloys, core-shell and contact aggregate which cannot be obtained from monometallic catalysts [17]. An electronic property (charge transfer) plays an important role in getting improved catalytic activity in BNPs. In the recent scenario, trimetallic nanoparticles (TNPs) are professional expertise than MNPs and BNPs due to their unique properties such as stability, catalytic activity [18]. Different physical and chemical methods have been used for the synthesis of NPs

including microwave, co-precipitation, hydrothermal, selective catalytic reduction, and microemulsion, etc. Au-Pt-Ag trimetallic nanocomposites have been synthesized using advantageous microwave dielectric heating because of its reaction controlling mechanism by using it the structural aspect [19]. Co-precipitation is one of the simplest techniques employed for the synthesis of nanoparticles in various forms like oxides, hydroxides, carbonates, and sulfides, etc. The precipitates are calcined to extract the powder form of TNPs at suitable temperatures. Trimetallic nanocomposites of CeO_2/ZnO/$ZnAl_2O_4$ have been synthesized by the co-precipitation technique [20]. A method of synthesis of single crystals depends on the solubility of nutrients in hot water under high pressure. For instance, trimetallic Pd-Ni-Al nanoparticles have been synthesized by hydrothermal technique [21]. The selective catalytic reduction can be used for the synthesis of mono to trimetallic nanoparticles. Pd-Co-Au has been synthesized by a micro-emulsion technique which is considered as a thermodynamically stable and isotropic system [22].

Nano-scaled metal oxide particles have received much attention due to their optical, electrical, and magnetic properties, which depend on the size and shape of the particles [23]. Oxide semiconductors containing metal atoms have a wide band gap resulting in the transmission of light in the visible spectrum. The energy distribution of electrons in semiconductors establishes the electrical and optical properties. In solid-state condensed matter, the electronic energy levels are arranged in a band structure. In semiconducting materials, the energy difference between the valence band and conduction band is the band gap of the material which determines the absorption of photons [24]. The exciton energy which governs the inception of vertical inter-band transitions is an optical band gap that differs from the minimum energy required to create an electron-hole pair (electrical band

gap). By opting suitable metal ions having various electropositive nature along with controlling the atomic chemical composition in mixed metal oxides, the band gap energy, as well as the spectroscopic properties, can be tuned. Mixed metal oxides have a catalytic activity in a heterogeneous manner [25]. In some cases, the cations in a mixed metal oxide can work jointly to catalyze different steps of a chemical process. The interaction of metal-metal or metal-oxygen-metal in mixed metal oxides can give rise to new electric states, which is not possible to get in single metal oxides. Nanocomposites of mixed metal oxide have varieties of applications in different research areas including catalysis and gas sensors, energy harvesting devices like fuel cells, photovoltaic devices (solar cells), and light-emitting devices [26]. Moreover, metal oxides are also useful in hydrogen production and its storage, purification of air and water by the degradation and adsorption of organic-inorganic pollutants/toxic gases, moisture and thermal sensors, UV-screening, and photodetectors. Besides, Metal oxide nanocomposites have stunning applications in biological and medical sciences such as drug delivery, cancer therapeutics, magnetic resonance imaging, and anti-microbial agents. Remarkable features of mixed metal oxide nanocomposites have been used as anti-corrosion applications [27].

1.2. Zirconium dioxide (ZrO_2) characteristic

ZrO_2 also known as zirconia, is a white color inorganic metal oxide that is commonly used in ceramic materials. Zirconium dioxide achieves as the compound of element zirconium (atomic number 40, atomic weight 91.22, density 6.49 g/cm^3, melting point 1855 ˚C, and a boiling point of 4409 ˚C) that exists in nature as heavy metal [28]. It has splendid characteristics like hardness, low reactivity, and a high melting point so that it

gains its acute attention to the researchers. ZrO_2 exists in mineral form as baddeleyite, a modified monoclinic crystal lattice. It has non-magnetic behavior and highly resistant against acids, alkaline nature and exogenous influences [29]. Due to the excellent properties such as low thermal conductivity, high thermal expansion coefficient, high thermal shock resistance, high oxygen ion conductivity, ZrO_2 uncovers extensive applications in catalytic supports, solid-state electrolytes, and functional coatings. It has a melting point of 2680 ˚C, that's why it is used in high-temperature ceramics such as crucible or furnaces. Likewise, it is very resistant to abrasion due to its high mechanical stability.

At atmospheric pressure ZrO_2 exists in three different crystalline polymorphs viz. tetragonal phase (t- ZrO_2) in the form of straight prism with rectangular sides (a = 0.3632 nm, c = 0.5057 nm), cubic phase (c- ZrO_2) in the form of straight prism with square side (a = 0.5128 nm), and monoclinic phase (m- ZrO_2) in the form of deformed prism with parallelepiped sides (a = 0.5128 nm, b = 0.5196 nm, c = 0.5316 nm, and $\beta = 98.83$) [30]. The cubic phase is stable above 2370 C and with mild mechanical properties, the tetragonal phase is stable between 1170 ˚C and 2370 ˚C with enhanced mechanical properties, and the monoclinic phase is stable at room temperature up to 1170 ˚C with lower mechanical properties. However, out of these three different crystal structures, the tetragonal phase is metastable but is widely used as catalytic support [31]. The stabilization of the tetragonal phase is done by doping the zirconia with other metal oxides like MgO, CaO, yttria. Yttrium stabilized zirconia (YSZ), also known as tetragonal ZrO_2, and glass-infiltrated zirconia-toughened alumina (ZTA) is broadly studied combinations in the recent

scenario. Their concentrations and transformation between three crystal structures depend on ZrO_2 doping and its thermal treatment.

Besides, every transition between the crystalline reticulations is anticipated to a force on the ZrO_2 surface, and this produces a volumetric change in the crystal where the stress is applied [32]. When stress occurs on the ZrO_2 surface, tetragonal to monoclinic transition takes place due to the energy cracking. The alteration from tetragonal to monoclinic phase could lead to a 3-5% volume expansion, enough to lead to catastrophic failure at a temperature starts from 950 ˚C with a reversible mechanism. Therefore, it is crucial to synthesize stable tetragonal ZrO_2 in the functional shielding coatings at benign temperature to prevent the expansion [33]. Different simple and versatile technologies such as plasma spraying, radio frequency (RF) magnetron sputtering, ion beam assisted deposition, pulsed laser deposition, sol-gel process, hydrothermal process, precipitation process, etc. have been employed for the synthesis of ZrO_2 material [34].

1.3. Titanium dioxide (TiO_2) characteristic

TiO_2, also known as titanium (IV) oxide, titania, titanic anhydride, titanic acid anhydride, titanium white or pigment white 6 in building paints, and E171 in food coloring, has been increased drastically because of its appositeness ranging from energy to environment to health [35]. Their significance in the current era and their efforts taken up for the advancement in its applications owes to its various features like plenitude, economical reasonability, non-toxicity, biocompatibility, high chemical stability, and corrosion resistance. At present, TiO_2 is being widely exploited for its photocatalytic and photovoltaic properties.

TiO_2 is a white non-combustible and odorless powder with a molecular weight of 79.9 g/mol, the boiling point of 2972 °C, a melting point of 1843 °C, a relative density of 4.26 g/cm^3 at room temperature and exists with many polymorphs. Anatase, rutile, brookite, and TiO_2 (B) are the four mineral forms of TiO_2 [35, 36]. The well-known crystal phase of TiO2 are naturally available rutile, anatase, and brookite, coined after their characteristic reddish color, extended crystallographic shape, and a mineralogist, respectively and they are the slight modification of TiO_6 octahedron so that corner- and edge-sharing of TiO_2 units is shown in rutile and brookite, where the same is shared in all three directions for anatase [36, 37]. The irreversible transformation of metastable anatase and brookite crystal phases to a stable rutile phase can be obtained upon the heating process. Moreover, TiO_2 has other eight modifications namely, three metastable phases (monoclinic TiO_2 (B) with group space of C2/m, tetragonal TiO_2 (H) with space group of I4/m and orthorhombic TiO_2 (R) with space group of Pbnm) and five high pressure forms (orthorhombic TiO_2 (II) with space group of Pbcn, monoclinic form with space group of P21/c, orthorhombic TiO_2-OI, cubic phase and orthorhombic TiO_2-OII). Among these phases, good symmetry is claimed for tetragonal anatase (I41/amd) and tetragonal rutile (P42/mnm) whereas orthorhombic brookite (Pbca) possess a low symmetry. Rutile and anatase demonstrate very similar physical properties with the existence of a slight difference [38].

Nanoparticles of TiO_2 are produced profusely and utilized widely because of their high stability, charge carrier, oxidizing power, non-toxicity, photocatalytic properties and anticorrosive properties [35, 36, 39]. Various factors such as shapes, size and special facets of TiO_2 nanomaterials also influence their applications. Rutile is the most stable phase,

while anatase is the most thermodynamically stable. TiO_2 receives its applicability in various fields such as dye-sensitized and quantum dot sensitized solar cells, water splitting, and general photo-catalysis, lithium-ion batteries, and supercapacitors, gas sensors, antifogging, deactivation of bacteria, paints, plastics, papers, inks, medicines, pharmaceuticals, food product, cosmetics, toothpaste, coatings, etc. TiO_2 is an n-type semiconductor with a band gap greater than 3 eV, its photocatalytic and photovoltaic applications is associated with its capability in light adsorption [40]. For example, a UV light will be absorbed by TiO_2 and an electron is excited to conduction band from the valence band, leaving behind a hole in the valence band, to form electron-hole pairs which can either be contributed to the photogenerated power or drive a chemical reaction, which is known as photo-catalysis. Due to the large band gap of TiO_2, there is rapid recombination of electron-hole pairs and the light adsorption is narrowed to the UV region. For the improved efficiency, modifications on the electronic structure of TiO_2 can be done because of its photocatalytic properties, can absorb high energy photons of ultraviolet radiation that destroy other materials by photochemical deposition (breaking chemical linkages). TiO_2 being an inorganic pigment, having luminosity and refractive index can improve physical, mechanical, and anti-corrosion properties by adding this white pigment to paint, coatings, catalysis systems, water purifier agents, etc, Due to its insolubility in water, various acids, and organic solvents, makes them more suitable as an anti-corrosive agent [41].

1.4. Zinc oxide (ZnO) characteristic

ZnO is one of the most engrossing groups II-VI compound n-type semiconductor material with a wide direct band gap (3.37 eV), high transmittance (> 80%) in the visible region and hexagonal wurtzite crystal structure [42]. It has large exciton binding energy (60 meV) at room temperature. ZnO exhibit high mechanical, chemical and thermal stability, and thus, has deep attention as an attractive material due to its versatility and potential applications for UV-light emitters, varistors, surface acoustic wave devices, transparent electrode for photovoltaic devices, optical waveguides, catalysis, flat panel display, chemical and gas sensor, anti-corrosion [42, 43]. The chemisorption of reducing gas molecules on the ZnO surface results in a decrease in the electrical resistance of oxide material. The non-stoichiometry associated with oxygen vacancy and/or donor states of metal in ZnO contributes to the electrons in the conduction band [44]. The chemisorbed oxygen traps conduction electrons and remains as negatively charged oxygen species (O^{--}, O^{-}, O^{2-}) on the surface increasing electrical resistance [44, 45]. In the presence of a reducing gas, the trapped electrons will be released resulting in a decrease in resistance of the material due to the reaction between the negatively charged chemisorbed oxygen species and the gas molecules. Various methods have been used to prepare zinc oxide nanoparticles by chemically such as hydrothermal, solvothermal methods, micro-emulsion, sol-gel, and thermal decomposition of precursors [46].

1.5. Scope and objectives

The natural phenomena of surface deterioration of metals/alloys within a particular environment are known as corrosion. According to the International Union of Pure and

Applied Chemistry (IUPAC) "Corrosion is an irreversible interfacial reaction of a material (metal, ceramic, and polymer) with its environment which results in the consumption of the material or dissolution into the material of a component of the environment. Often, but not necessarily, corrosion results in effects detrimental to the usage of the material considered. Exclusively physical or mechanical processes such as melting or evaporation, abrasion or mechanical fracture are not included in the term corrosion" [47]. This process is believed as detrimental, i.e. the deterioration/disintegration that occurs with corrosion, however, it is important to be noted that there are abundant beneficial uses regarding corrosion. Electrochemistry and thermodynamics are crucial for understanding the corrosion and its control mechanism. The mechanism of anti-corrosion can be categorized into three, namely, a barrier between material and environments, inhibition of corrosion process, and coating as surface materials. Among them, coating a surface material have been investigated effectively. Coating materials can be organic, inorganic, or metallic. Relatively thin coatings of metallic and inorganic materials are always imperative because it provides the path for effective utilization of barrier between the metal and its environment. Coating by the more scientific way including a physical vapor deposition system can enhance the quality of barrier film and reducing the cost of coating materials by the utilization of less quantity and minimization of losses of expensive coating materials.

In this study, we have synthesized a novel tri-metallic nanocomposite of transition metals with different compositions based on ZrO_2/ZnO/TiO_2 by mechanochemical process and an ultra-thin coating was performed via radio frequency magnetron sputtering on different substrates. The preparation of trimetallic nanocomposite by ball milling in different compositions and coating done via RF sputtering under the different experimental

conditions are the novelty of the work. Moreover, electrochemical impedance spectroscopy (EIS) analysis was performed to understand the functioning of corrosion resistant.

2. EXPERIMENTAL SECTION

2.1. Materials

Zirconium (IV) oxide powder, 5 µm, 99.0 % trace metals basis, Titanium (IV) oxide, anatase powder, 99.8 % trace metals basis were purchased from Aldrich chemistry. Zinc oxide, powder, <5 micron, 99.9 % and triton-100 were obtained from Sigma-Aldrich and used without further purification. Sodium hydroxide (NaOH), hydrochloric acid (HCl) (ACS reagent, 37 %) were supplied by Sigma-Aldrich (chemicals company), while Extran and ethanol (99.9 %) solutions were purchased from Merck and J.T. Baker. Nitrogen (N_2) gas cylinder was purchased from INFRA, Mexico. Carbon steel (CS) (PROMINOX, 0.6 mm thickness) were used as a substrate. Stainless steel (SS) was purchased from Q-panel. Sodium chloride (NaCl) was purchased from VWR.

2.2. Synthesis of tri-metallic oxide powder

The mechanochemical process (ball milling) was utilized for the synthesis of trimetallic (ZrO_2/ZnO/TiO_2) powder by varying the different compositions. Mechanical alloying is a solid-state powder processing technique as shown in Fig. 1. It is a high-energy ball milling technique that involves repeated welding, fracturing, and rewelding of powder particles. The recognition of the possibility of mechanically induced chemical reactions in the powder mixture made this process more interesting. Mechanochemical synthesis is a general term given to the mechanical alloying process in which chemical reaction takes place during milling of metal powders. Production of fine dispersion of second phase (usually oxide) particles, extension of solid solubility limits, refinement of grain sizes

down to nanometer range, synthesis of novel crystalline and quasi-crystalline phases, combustion reactions, refining of metals, possibility of alloying of difficult to alloy elements, inducement of chemical (displacement) reactions at low temperatures, scalable process. However, the principal components of the mechanochemical process are raw materials, type of mill and process variables. It includes milling speed, milling time, a ball to powder ratio, milling container, type of mill, the size of the grinding medium, the extent of milling, milling atmosphere, the temperature of milling and process control agent.

Figure 1. Fritsch pulversite planetary mill

During the mechanochemical process, deformation is introduced into the particles through crystal defects such as dislocations, vacancies, stacking faults and increased number of grain boundaries. This defect structure aids for proper alloying by enhancing the

diffusivity of the elements into the matrix. Also, the properties of refined microstructure particles are such that it decreases the diffusion distance. Moreover, a small increase in temperature of the vial during milling assists the diffusion behavior. Tungsten Carbide vial is used as the container and 10 mm diameter Tungsten Carbide balls weighing 7.738 g are used as milling media. As-received ZrO_2, ZnO, and TiO_2 raw oxide powders were mixed in different stoichiometry (Zr rich to Zr poor) and then transferred to the milling process. The synthesized nanocomposite powders are listed in Table 1.

Table 1. Composition of ZrO_2/ZnO/TiO_2 nanocomposite powder

Sample designation	ZrO_2/ZnO/TiO_2 composition (wt%)		
	ZrO_2	ZnO	TiO_2
N1	90	5	5
N2	80	10	10
N3	65	10	25
N4	50	10	40
N5	40	10	50
N6	10	80	10

2.3. Target preparation

For voluminous processing of materials, it is expected to keep out a massive preliminary work to determine the synthesis parameters. Once these are established, a die of suitable dimension is prepared, and the powders are condensed and sintered under sensibly controlled conditions. In the case of sputter targets, the use of hot-press makes

easier this process as it guarantees regulated densification with proper dimension. Where the hot-press is not available, it is necessary to revert to the conventional practice of compaction. Sputter targets, especially for research and development purposes, is of low volume, but with rigorous requirements. The synthesized powder was mixed with triton-100 solvent to make it self-adhesive and manually pressed on the copper base plate followed by drying at 100 ˚C in the normal oven for 12 hr. 3 hr milled nanocomposites with different compositions were utilized for the target preparation.

2.4. Nanocomposite coating preparation

Radio Frequency Sputtering is the technique involved in alternating the electrical potential of the current in the vacuum environment at radio frequencies (generally 13.6 MHz) to avoid a charge building up on certain types of sputtering target materials, which over time can result in arcing into the plasma that discharges droplets creating quality control issues on the thin films and can even lead to the complete termination of the sputtering of atoms ending the process as shown in Fig. 2. The target to substrate distance was fixed at 3.5 cm. The chamber was evacuated to a base pressure of 5.5×10-6 Torr by a turbo-molecular pump before the deposition to eliminate the residual gases present inside the chamber. Ar gas was used as the working gas. Substrates temperature were fixed intentionally at 150 ˚C during the deposition process. Coatings were done at varying RF power (100, 120, and 140 W) for getting ultra-thin films at a working pressure of 15 mTorr. The rotation of the substrate holder was fixed to 6 rpm throughout all the deposition to get lateral uniformity.

Figure 2. RF magnetron sputtering PVD system

2.5. Characterization techniques

The crystallinity, crystallite size and phase assessment of the samples was carried out using X-ray diffraction (XRD) recorded on a D2 phaser diffractometer using Cu- Kα (λ=1.5406 Å) radiation. The absorption coefficient (α) was calculated from the transmittance data, and the Tauc plot was used to determine the bandgap of the films. The micro Raman spectra of fabricated samples were obtained by the HORIBA Jobin Yvan system with He-Ne laser (632 nm) at room temperature. The morphological studies were carried out using the TESCAN VEGA scanning electron microscope (SEM) and Auriga field emission scanning electron microscope (FESEM) on the surface of the deposited films. The chemical composition of the samples was examined using an electron dispersive x-ray spectroscopy (EDS) coupled with SEM.

2.6. Electrochemical measurements of nanocomposite coated carbon steel

Electrochemical impedance spectroscopy (EIS) measurement was performed by using a three electrode cell system which consists of platinum (Pt) mesh counter electrode (CE), saturated calomel electrode (SCE) reference electrode (RE) and carbon steel plate as a working electrode (WE). The measurements were carried out with a Potentiostat/Galvanostat (Gamry interface 1010). The samples were exposed to NaCl solution for 10 days at room temperature. The exposed area of each samples is 2.714 cm2. Each set of measurements included 6 min of open circuit potential (OCP) followed by potentiostatic EIS with a range of frequencies between 10^5 and 0.03 Hz (10 points per decade interval) and an amplitude of 10mV (rms). The results of the EIS experiment were fitted in Gamry® software.

3. RESULTS AND DISCUSSION

3.1. Characterizations of powder sample

In the results and discussion section, we start the analysis of Zr-rich ZrO_2/ZnO/TiO_2 (80/10/10) trimetallic oxide powder samples as a function of different milling time and compositions and followed by the characterizations of coating films. Samples on the CS and SS substrates were used to analyze the morphological and physical properties.

3.1.1. Structural properties

X-ray diffraction is a powerful technique to understand the structural properties of materials. Fig 3 shows the XRD patterns of ZrO_2/ZnO/ TiO_2 (80/10/10) trimetallic oxide nanocomposites milled for different timing (3 hr to 17 hr) with a polycrystalline. The sample milled for 3 hours showed more peaks corresponding to single ZrO_2, ZnO, and TiO_2 metal oxide. The diffraction peaks in the spectra for 3 hr are dominantly indexed to monoclinic (baddeleyite) ZrO_2 and in close agreement with those of standard data (JCPDS card # 37-1484) [48]. The strongest diffraction peak at around 28.4˚ corresponds to the (-111) reflection plane. A reflection plane (011) at around 31.7˚ belongs to anatase TiO_2 crystal structure [49]. The peaks at the scattering angle (2θ) of 34.5 correspond to the reflection from (002) crystal plane which is identical to the hexagonal crystal phase with Wurtzite structure [50]. Distinct evidence of milling time can be seen in the XRD spectra of Zr-rich trimetallic nanocomposites. Multiple peaks corresponding to single metal oxide reduced significantly with increased milling time due to inter-diffusion of phased during

mechano-chemical processing leading to the enhancement in solid reaction. The intensity of preferential orientation fit into (-111) reflection plane was decreased and finally disappeared to the sample milled for 17 hr owing to the bimetallization/trimetallization forming a ternary/quaternary phases. Oxide composite of the Zr/Ti bimetallic phase was observed at a 2θ value of 30.8 corresponding to (311) reflection plane having a orthorhombic crystal structure. Similarly, Zn/Ti bimetallic oxide composite phase was observed at 35.5˚. Likewise, the reflection plane at 2θ 38.8˚ indexed to (511) represents the bimetallic oxide composite of Zr/Zn milled only for 3 hr. The intensity of Zn/Ti bimetallic oxide composite was increased with milling time owing to the enhancement in crystallinity. The crystallite size increased from 12.3 nm for 11 hr of milling time to 18.7 nm for 17 hr of milling time calculated from (311) reflection plane at 2θ = 30.8˚ by using the Scherrer equation. Only four preferential peaks corresponding to one Zr/Ti, one Zn/Ti, and two ZrO_2 were observed for the samples milled for 15 hr and 17 hr as shown in Fig. 3.

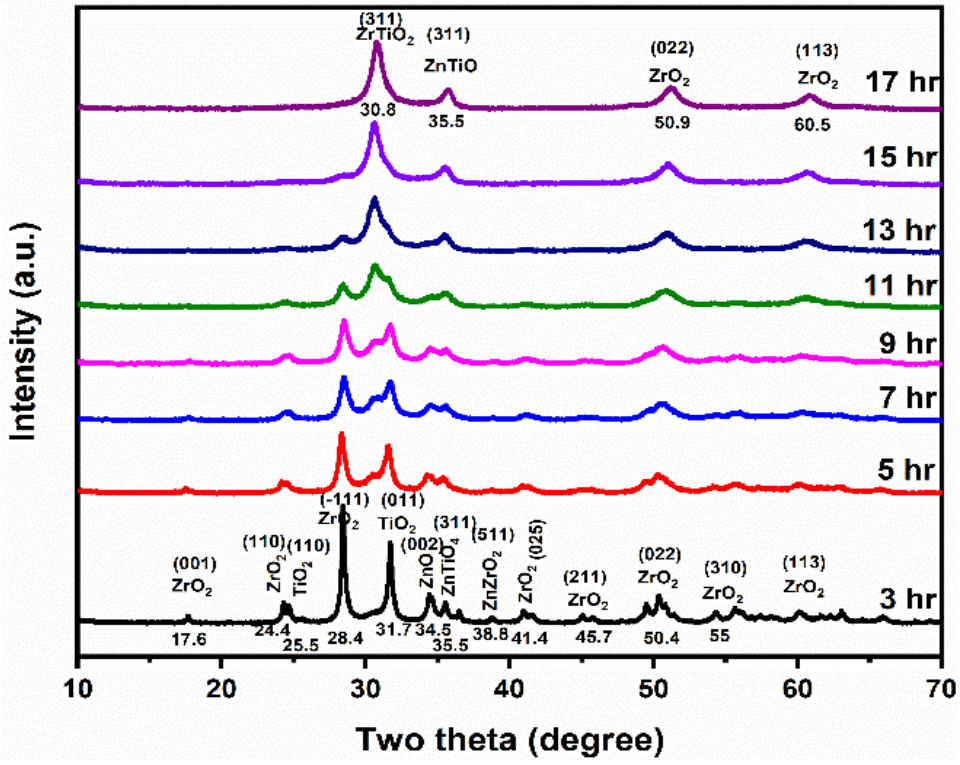

Figure 3. XRD patterns of ZrO_2/ZnO/TiO_2 (80/10/10) trimetallic oxide nanocomposites of powder samples synthesized for different milling time.

XRD pattern of trimetallic oxide nanocomposite with different compositions milled for 3 hr is shown in Fig. 4. The intensity of reflection plane (-111) corresponds to monoclinic ZrO_2 was decreased while decreasing the composition of Zr. Reflection plane (011) corresponds to TiO_2 phase in the XRD pattern. Hexagonal crystal structure with a reflection plane (002) belongs to ZnO phase indicated the c-axis perpendicular to the plane.

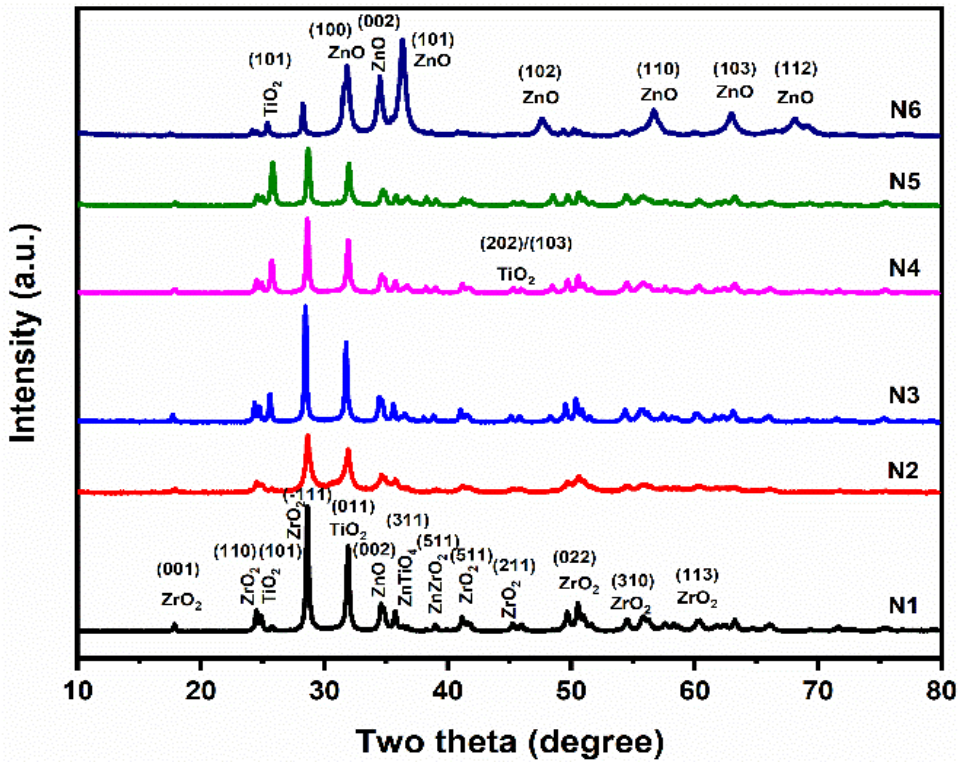

Figure 4. XRD patterns of trimetallic oxide nanocomposites with different compositions milled for 3 hr

Raman spectroscopy is a very sensitive and non-destructive technique for investigating semiconducting materials. The processing of composite particles in high energy mills, also called mechanical activation, is a very efficient and cost-effective method for the preparation of materials at the nanoscale level. Raman spectroscopy technique can be applied to investigate the microscopic nature of structural as well as morphological disorder. Raman shift at 152 cm^{-1} and 187 cm^{-1} are the strongest mode observed due to the vibration of zirconium atom along with oxygen atoms and are assigned to Ag peak mode as shown in Fig. 5. In monoclinic ZrO_2, each Zr atom is surrounded by

seven oxygen atoms with the Zr-O distance between 2.159Å [51]. The intensity and narrowness of the strongest peak determine the degree of formation of a crystal structure. With the increment of milling time from 3 hr to 17 hr, a distinct pattern of Raman spectra can be observed due to bimetallic composition phases, that is, the dominancy of the strongest peak of single metal oxide become weak.

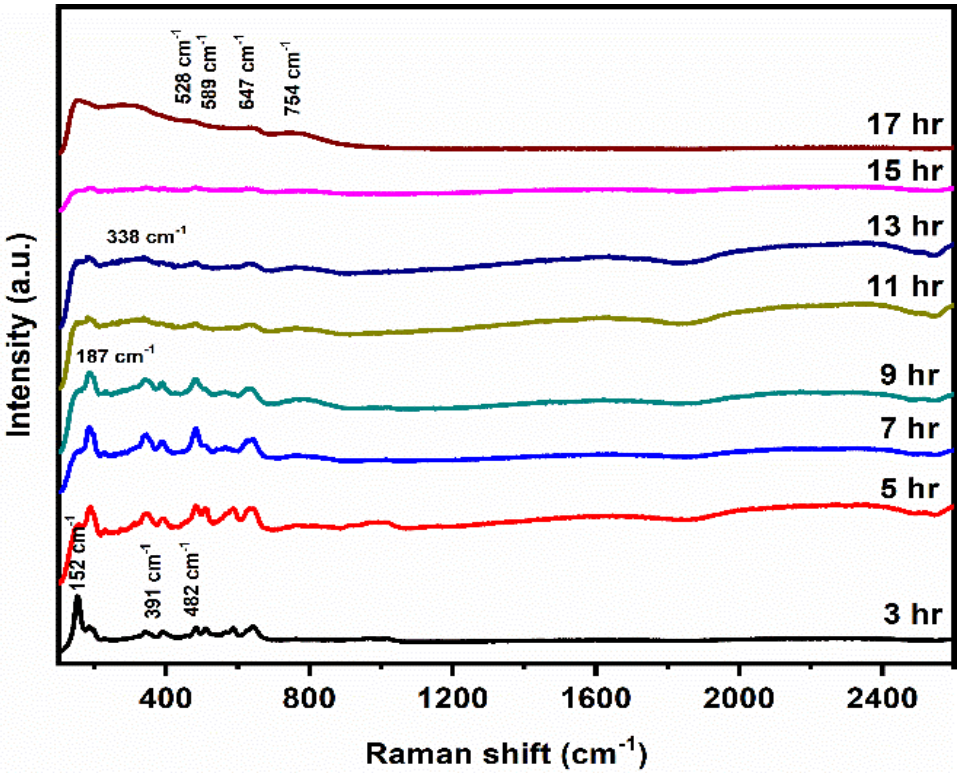

Figure 5. Raman spectra of $ZrO_2/ZnO/TiO_2$ (80/10/10) trimetallic oxide nanocomposites of powder samples synthesized for different milling time.

3.1.2. Morphological and compositional properties

Mechanical milling is a process of repeated flattening, cold wedding, fracturing, and rewelding of powder particles. The ductility and the brittleness of the particle system explains the formation morphology during the milling process which leads to the deformation and fragmentation, respectively. The morphologies of the ball milled samples are displayed in Fig. 6a-h corresponding to different milling times from 3 hr to 17 hr. The clear indication of the mechanical activation energy as an effect of milling time can be observed on the morphology of prepared trimetallic oxide nanocomposites with the formation of agglomerates ranging from small to large. The density of particles increased while increasing the milling time owing to the better powder packing. The powder sample synthesized for short milling times showed spherical morphology with a predominance of deformed particles. The morphology became different grains with welded particles having overlapped structure. The morphological transformation took place to the randomly oriented particles at higher milling times. Powder milled for higher times exhibits broken pieces of flat-like structures which is taken into the bulk of the powder with heavily agglomeration. Agglomeration is an inherent property of the mechanically milled particles. The tendency to agglomerate increases as fractured particles have gained high surface energy. High surface energy and cohesion amongst particles with shrinking particle size account for agglomeration. The fracturing and cold-welding mechanism continue as milling time persists.

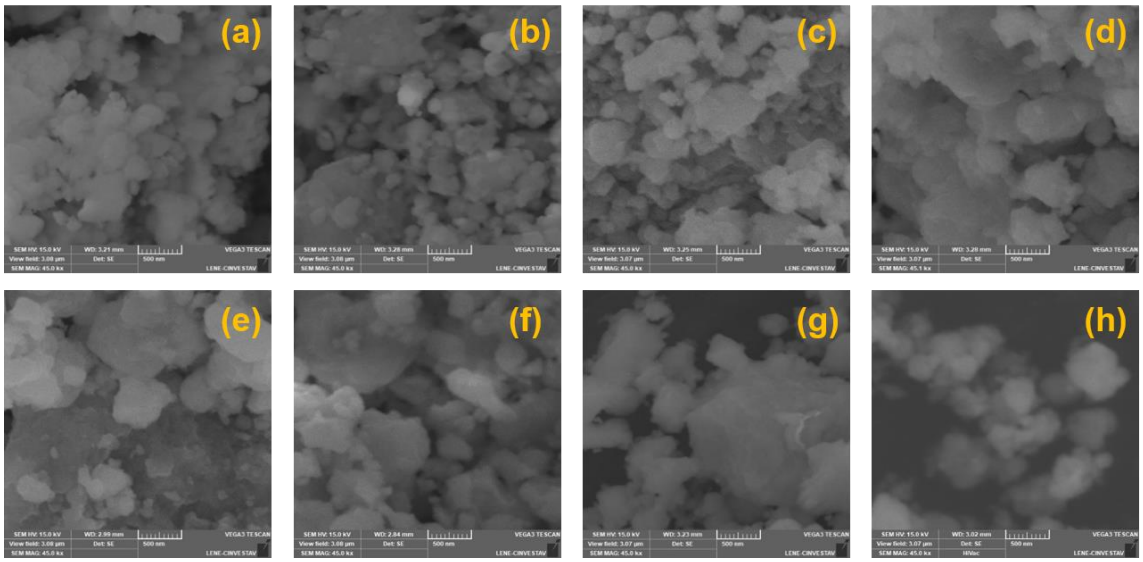

Figure 6. SEM images of ZrO_2/ZnO/TiO_2 (80/10/10) trimetallic oxide nanocomposites of powder samples synthesized for different milling time (a) 3 hr, (b) 5 hr, (c) 7 hr, (d) 9 hr, (e) 11 hr, (f) 13 hr, (g) 15 hr, and (h) 17 hr

The morphology of the powder sampled milled for 3 hr with different compositions can be shown in Fig. 7. The grain size of the nanocomposites was increased with increasing Zr composition having a formation of agglomeration. The powder sample having Zn rich composition showed highly dense agglomeration of the nanocomposites. Distinct evidence of the morphology can be seen from different compositions of trimetallic oxide nanocomposites. The elemental distribution in the synthesized powder with different compositions milled for 3 hr can be seen in Fig. 8.

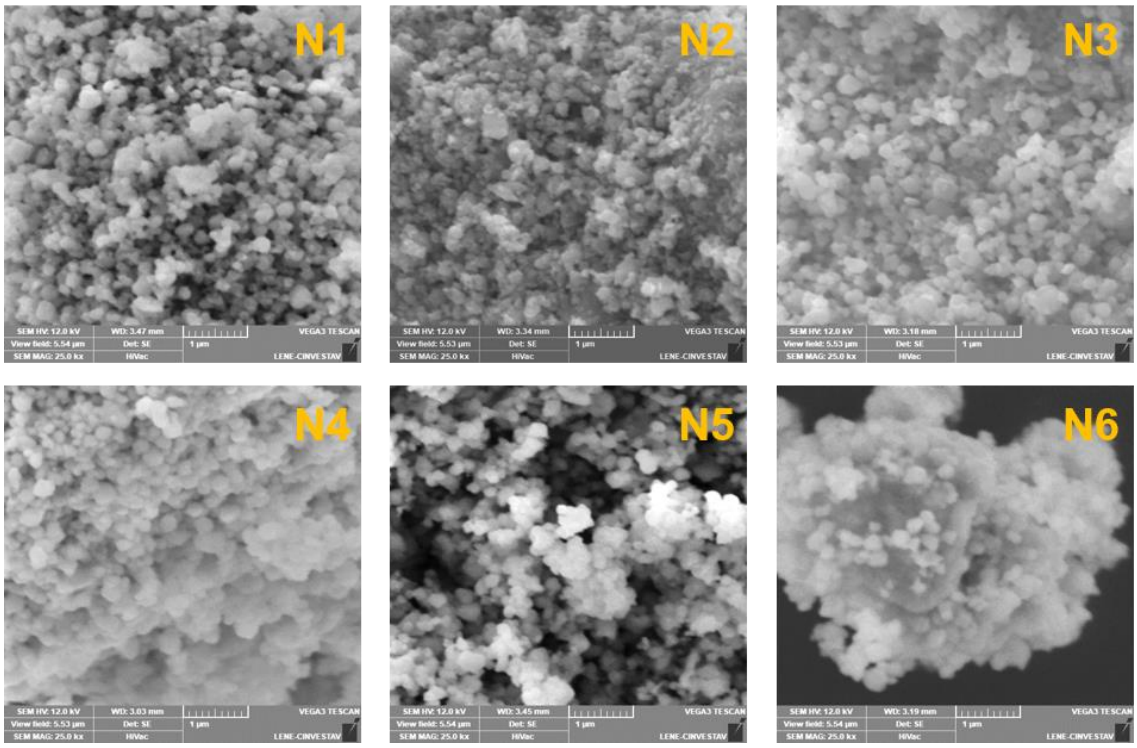

Figure 7. SEM images of trimetallic oxide nanocomposites of powder samples with different wt% compositions of ZrO_2/ZnO/TiO_2 milled for 3 hr

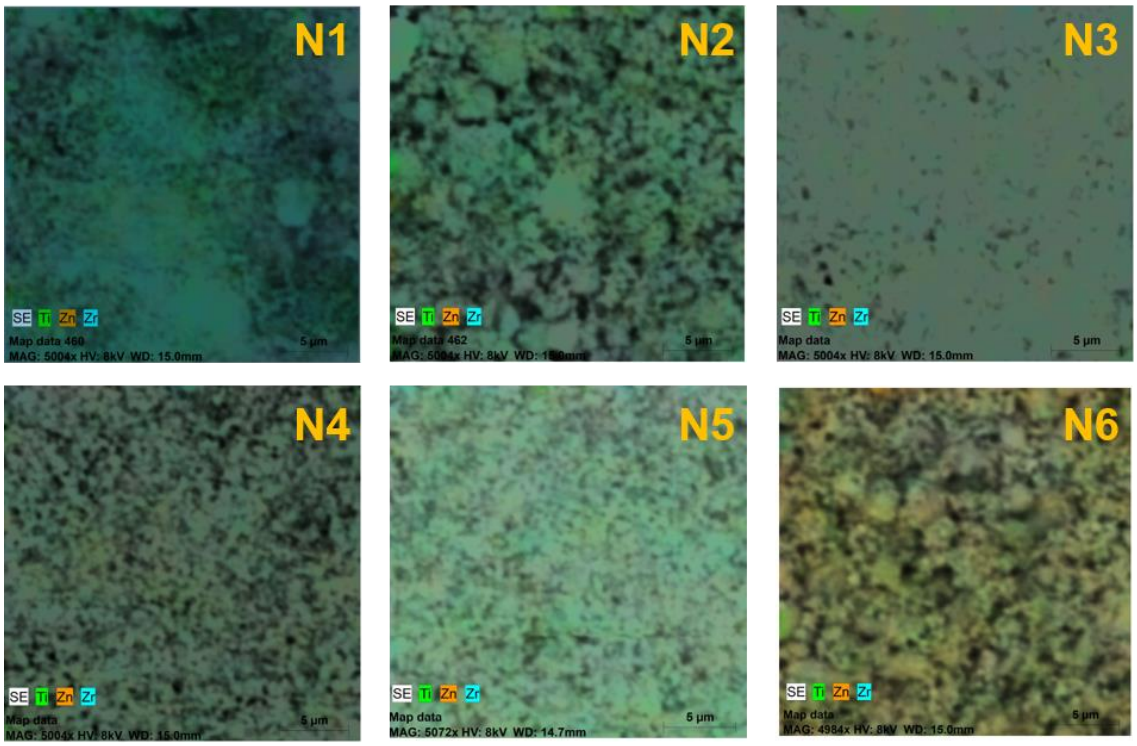

Figure 8. Mapping images of trimetallic oxide nanocomposites of powder samples with different wt% compositions of ZrO_2/ZnO/TiO_2 milled for 3 hr

Energy dispersive X-ray spectroscopy (EDS) analysis shows the presence of quantitative compositional information of the elements present in trimetallic oxide nanocomposites. Fig. 9 represent the EDS of ball milled samples with different milling time (3 hr to 17 hr). EDS spectra show the peaks of zirconium (Zr), titanium (Ti), and zinc (Zn) along with the extra peaks of oxygen and carbon (from the sample holder). The quantitative analysis of all the elements can be shown in Table 2. The quantitative composition of zirconium was decreased with the increased milling time owing to the composite formation due to mechanical activation energy. Since milling time is short, the

distribution of elements in the powder is not completely homogenous. But as the milling time prolongs, the elements alloy distributed homogenously. Hence, it is clear that milling time has an influence on the homogeneity on milled powder.

Table 2. EDS analysis of ZrO_2/ZnO/TiO_2 (80/10/10) trimetallic oxide nanocomposites of powder samples synthesized for different milling time

Milling time (hr)	Oxygen (at. %)	Carbon (at. %)	Zirconium (at. %)	Zinc (at. %)	Titanium (at. %)
3	23.64	64.62	9.58	1.09	1.07
5	23.47	62.54	9.59	1.95	2.47
7	31.68	55.81	9.32	1.31	1.89
9	26.51	61.51	8.77	1.37	1.84
11	26.51	63.26	7.54	1.22	1.48
13	14.74	76.79	6.50	0.71	1.26
15	24.38	66.27	7.03	0.86	1.46
17	22.38	69.35	6.23	0.92	1.12

3.2. Characterizations of coating film

In this section, we have discussed the results about the RF sputtered ultra-thin film (~50 nm) on CS and SS substrates fabricated from the sputtering target for the powder samples milled for 3 hr with varying composition from Zr rich to Zr poor. The presented results are for those samples which were sputtered at RF power of 120 W, substrate temperature of 150 ˚C, 3.5 cm substrate to target distance, Ar as working pressure, and 15 mTorr of working gas pressure. Raman spectroscopy, morphology, mapping images were taken on stainless steel samples

3.2.1. Structural analysis

Raman spectroscopy has been proved a good technique for the analysis of metallic oxides. Mechanical activation introduces lattice disorder and extended defects into the crystal structure, and the understanding of these changes is of both practical and theoretical interest. The phase transformation could be the possible fact after sputtering. A slight difference in the Raman spectra of the ultra-thin film was observed than the Raman spectra of the powder sample of trimetallic oxide nanocomposites. Raman scattering can give important information about the nature of the solid on a scale of a few lattice constants. Raman shift at 347 cm^{-1} and 395 cm^{-1} correspond to B_g mode while raman shift at 487 cm^{-1}, 570 cm^{-1}, and 645 cm^{-1} assigned to A_g mode as shown in the Raman spectra of prepared samples (Fig. 10) predominantly belongs to ZrO_2 [52]. Similar patterns of Raman spectra can be observed for other Zr rich samples. More peaks compared to Zr rich films can be seen to the Zn rich ultra-thin coating films.

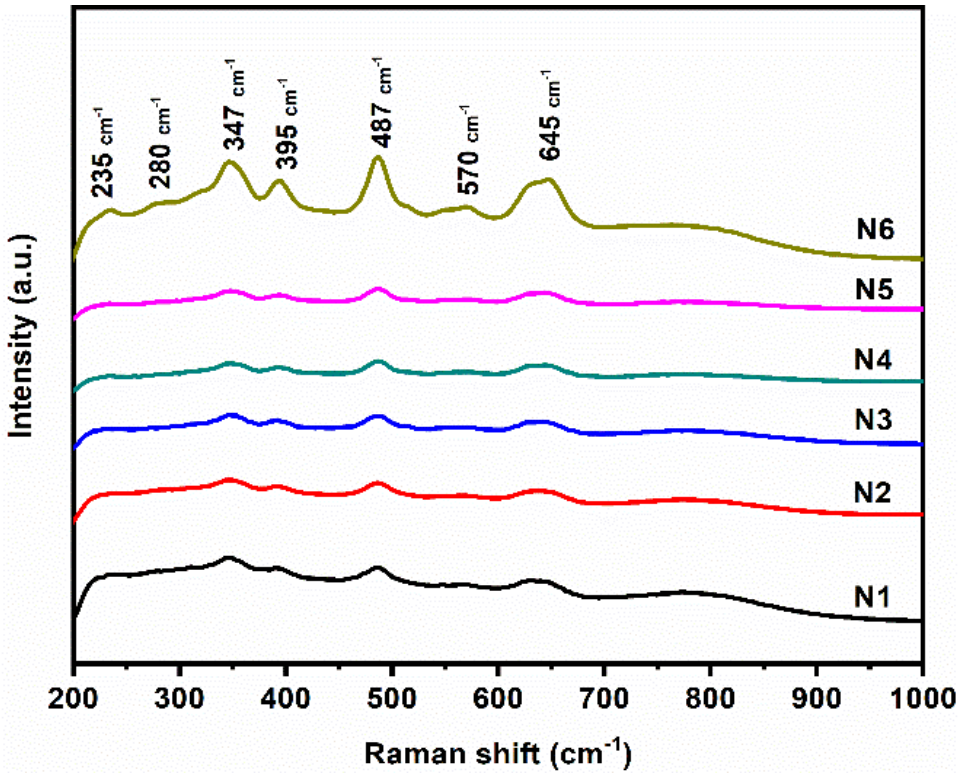

Figure 9. Raman spectra of RF sputtered (120 W) ultra-thin films of ZrO_2/ZnO/TiO_2 trimetallic oxide nanocomposites synthesized from 3 hrs of milling time with weight % composition

3.2.2. Morphological and compositional analysis

Fig. 10 (N1) - (N6) shows the FESEM images of ultra-thin films deposited by RF sputtering at 120 W by varying the elemental composition during the powder synthesis from ZrO_2/ZnO/TiO_2 based oxide nanocomposites. The grain size distribution of the sputtered films reveals compactness with well facetted with an average grain size of 22 nm. The morphology of the films from Zr-rich trimetallic oxide composite N1, N2, and N3 showed larger grains distribution than comparison to N4 and N5. Sample N6 revealed the

different morphology with enlarged grains distribution having an average grain size of 26 nm. The formation of uniform and crack-free morphology is an indication of effective coating performance for corrosion resistant application.

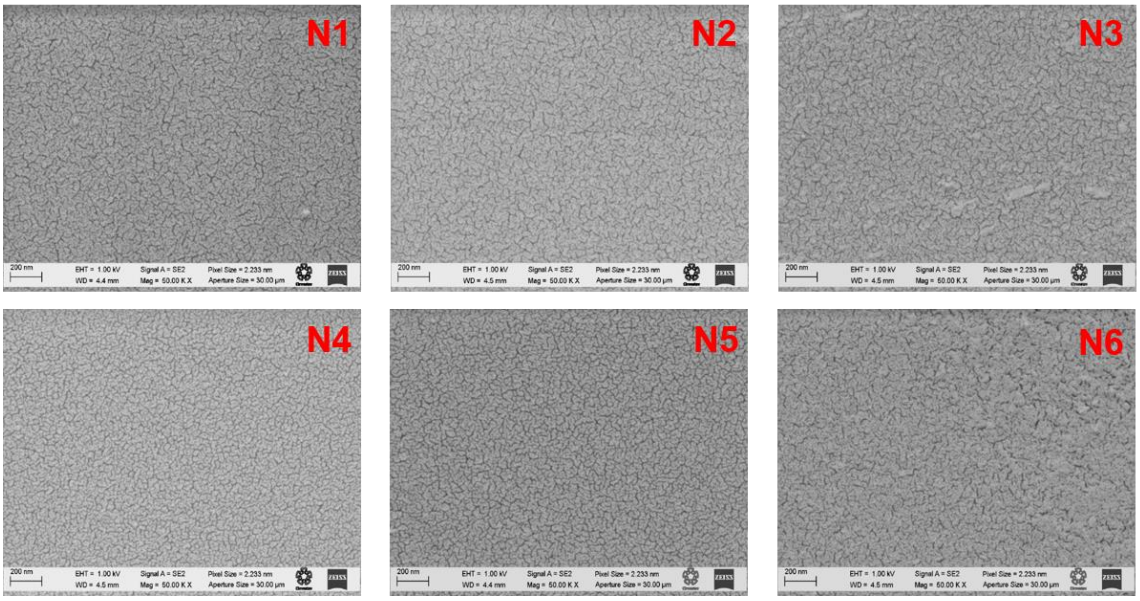

Figure 10. FESEM images of RF sputtered (120 W) ultra-thin films of ZrO_2/ZnO/TiO_2 trimetallic oxide nanocomposites synthesized from 3 hrs of milling time with weight % composition.

The elemental distribution in the entire film is an important feature to functionalize the material to its application part. Mapping images of such elemental distribution can be observed from the SEM micrograph as shown in Fig. 11. The divergent information of the elemental distribution to the prepared ultra-thin films can be visualized simply from the mapping images which is also an indication of uniformity of the films.

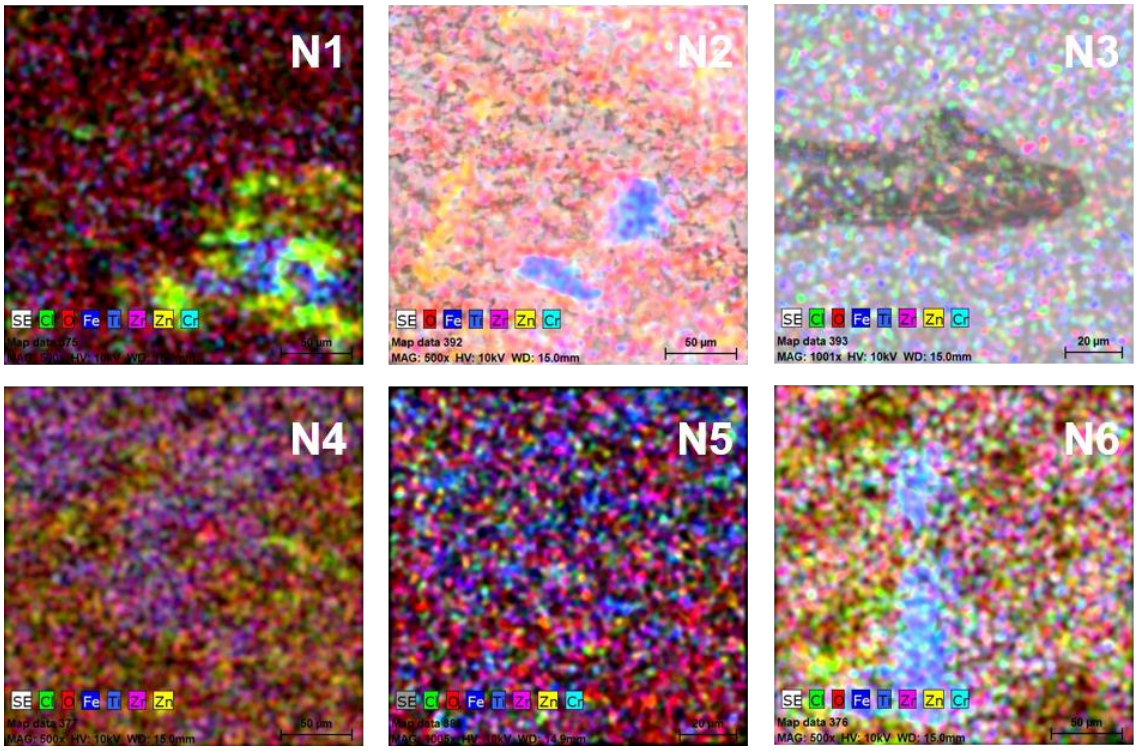

Figure 11. SEM mapping images of RF sputtered (120 W) ultra-thin films of ZrO_2/ZnO/TiO_2 trimetallic oxide nanocomposites synthesized from 3 hrs of milling time with weight % composition.

3.2.3. Electrochemical study of tri-metal oxide nanocomposite coated carbon steel

Corrosion behavior of CS substrate coated by nanocomposites of tri-metal oxide was investigated by using electrochemical impedance spectroscopy. To obtain more highly denser surface morphology of coating later, it was conducted additional process both RF power variation and thermal annealing treatment. Samples thus prepared were listed in Table 3.

Table 3. $ZrO_2/ZnO/TiO_2$ nanocomposite coated carbon steel (CS)

Sample designation	$ZrO_2/ZnO/TiO_2$ composition (wt%)				
	ZrO_2	ZnO	TiO_2	[a]RF (W)	[b]T (^oC)
CS1	-	-	-	-	
CS2	80	10	10	100	400
CS3	80	10	10	120	400
CS4	80	10	10	140	400
CS5	10	80	10	100	400
CS6	10	80	10	120	400

a: Radio frequency power (W)

b: Annealing temperature (^oC)

To show clearly the spectrum of capacitor and resistor for these systems, the impedance (|Z|) and Bode phase angle results based on electrochemical impedance measurement for CS as a bare sample and $ZrO_2/ZnO/TiO_2$ nanocomposite coated CS immersed in NaCl solution are presented as a function of different composition in Fig. 12. In Fig. 12(a), the |Z| of CS2 sample coated by $ZrO_2/ZnO/TiO_2$ exhibits higher values about 3 times than that of uncoated CS1 at the low frequency region after 10 day immersion. A capacitor and resistor can be combined in different ways with rather different effects. If the connection of capacitor and resistor is serial, which resembles a perfect coating. The capacitors impact increases with decreasing frequency.

Furthermore, the phase angle values of CS1, CS2 and CS3 samples exhibited at about -20°, -48° and -42°, respectively, when shifting toward lower frequencies as shown

in Fig 12(b). A purely resistive impedance will have a phase angle value of 0°, while a purely capacitive impedance will have a phase angle one of -90°. Based on phase angle values, the systems of CS2 and CS3 coating samples immersed in solution showed higher phase angle value than bare CS1. This might be attributed to highly denser structure of CS2 and CS3 as shown by SEM images in Fig. 10, which provide potential barrier with double layer capacitor of coating layers at the interface between metal substrate and electrolyte. Interestingly enough, the phase angle values of 80/10/10 samples regardless of RF power magnitude showed coating behavior with a relatively homogeneous distributed morphology and smooth surface, which enhance the barrier protection performance on the CS substrate.

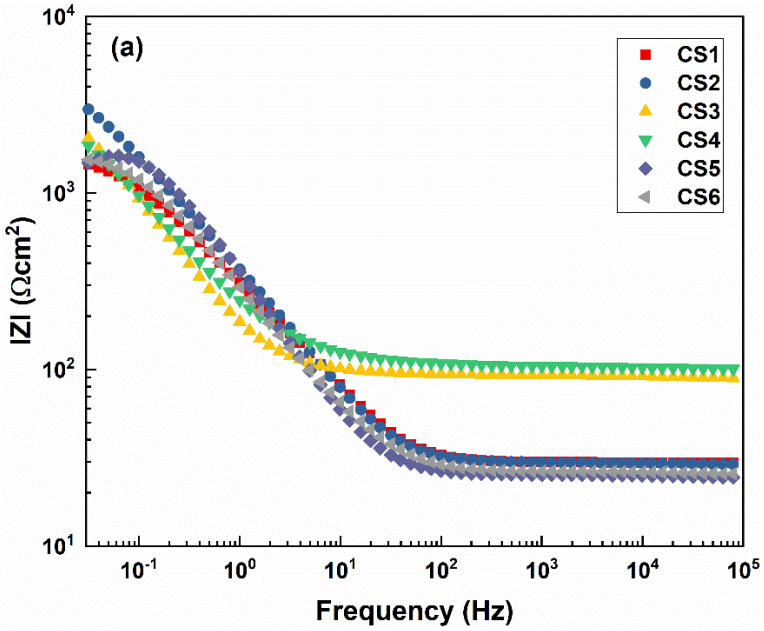

Figure 12. Impedance (a) and phase angle (b) results of ZrO_2/ZnO/TiO_2 nanocomposites coated CS as a function of composition with frequency sweep mode after 10 days immersed in NaCl solution.

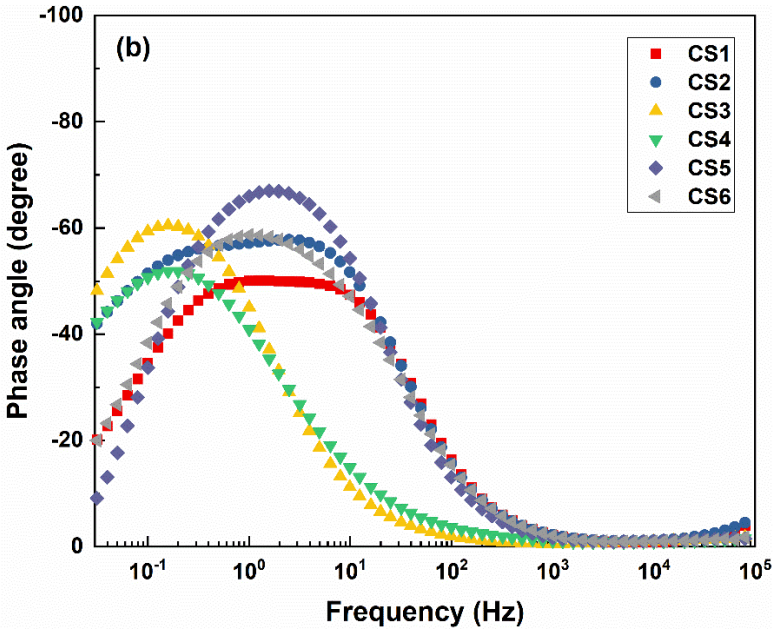

Figure 12 Continued.

The Nyquist plots based on EIS measurement for CS as a bare sample and $ZrO_2/ZnO/TiO_2$ nanocomposite coated CS immersed in NaCl solution are presented as a function of different composition in Fig. 13. The capacitive arc radii of bare sample CS1 decreased rapidly at low frequency region after 10 days of immersion. The charge transfer process occurred at the interface between the electrolyte and the CS substrate. It is revealed that the corrosion reaction of CS surface at the middle immersion stage is controlled by charge transfer. The CS2 and CS3 samples showed increase of phase angle in the coordinate and that of impedance magnitude which means excellent corrosion protection behavior of tri-metal oxide nanocomposites on CS substrate.

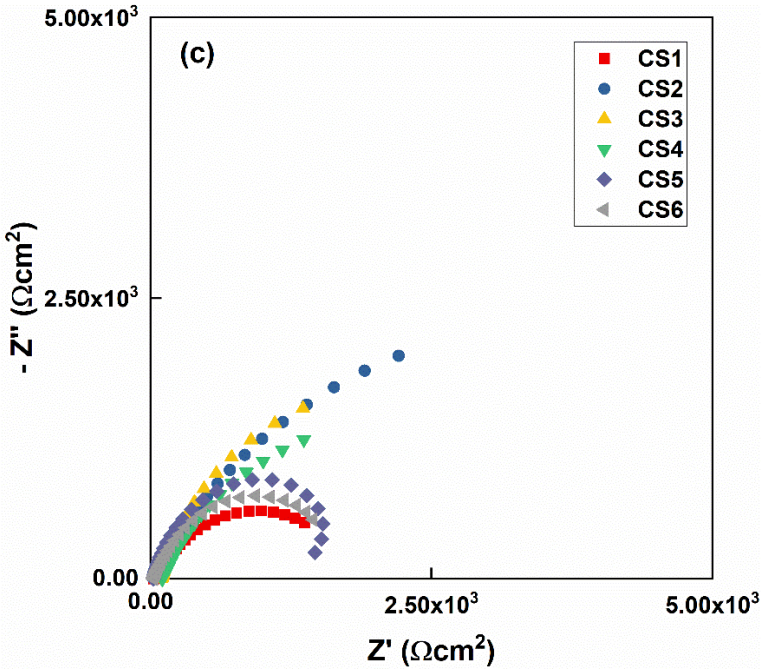

Figure 13. Nyquist plots of ZrO_2/ZnO/TiO_2 nanocomposites coated CS as a function of composition after 10 days immersed in NaCl solution.

3.2.4. Electrochemical study of tri-metal oxide nanocomposite coated stainless steel

To observe corrosion behavior, SS substrate coated by nanocomposites of tri-metal oxide based on ZrO_2, ZnO and TiO_2 were performed by using electrochemical impedance spectroscopy. Samples thus prepared were listed in Table 4.

Table 4. $ZrO_2/ZnO/TiO_2$ nanocomposite coated stainless steel (SS)

Sample designation	$ZrO_2/ZnO/TiO_2$ composition (wt%)				
	ZrO_2	ZnO	TiO_2	RF[a] (W)	T[b] (^oC)
SS1	-	-	-	-	
SS2	90	5	5	100	400
SS3	80	10	10	120	400
SS4	50	10	40	140	300
SS5	50	10	40	140	400
SS6	40	10	50	120	400
SS7	10	80	10	120	400

a: Radio frequency power (W)

b: Annealing temperature (^oC)

To show corrosion protection behavior of nanoomposite coatings, the impedance (|Z|) and Bode phase angle results based on electrochemical impedance measurement for bare SS and $ZrO_2/ZnO/TiO_2$ nanocomposite coated SS immersed in NaCl solution are presented as a function of different composition in Fig. 14. In Fig. 14(a), the |Z| of SS4 showed higher values about 4 times than that of uncoated SS1 at the low frequency region after 10 day immersion. A capacitor and resistor can be combined in different ways with rather different effects. If the connection of capacitor and resistor is serial, which resembles a perfect coating.

In addition, the phase angle value of SS4 and SS7 samples exhibited about -81° and -82° when shifting toward lower frequencies as shown in Fig 14(b). This might be

attributed to highly denser structure of 50/10/40 and 10/80/10 coatings on SS, which provide strong barrier protection with double layer capacitor at the interface between metal substrate and electrolyte. Perfect coating behavior of SS4 and SS7 samples was originated from a relatively homogeneous distributed morphology and smooth surface, which enhance the barrier protection performance on the CS substrate. A previous study has reported that Zn-doped Zn-ZrO_2/TiO_2 nanocomposite coating layers showed highly dense pore surface with no cracks [53]. Metal oxide elements in mapping images were also observed with homogeneous distribution morphologies in nanocomposite coating layer as shown in Fig. 11.

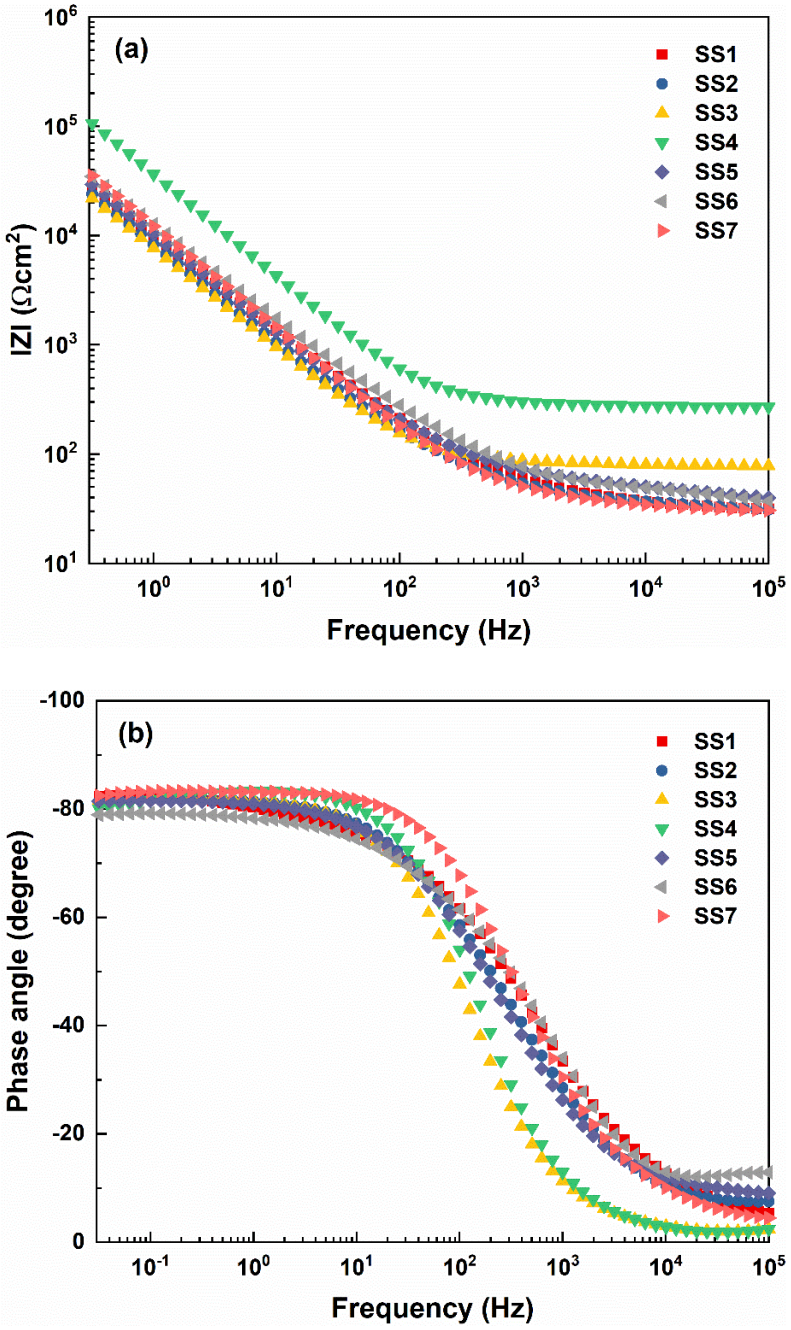

Figure 14. Impedance (a) and phase angle (b) results of $ZrO_2/ZnO/TiO_2$ nanocomposites coated SS as a function of composition with frequency sweep mode after 10 days immersed in NaCl solution.

The Nyquist plots based on EIS measurement for SS as a base sample SS1 and $ZrO_2/ZnO/TiO_2$ nanocomposite coated SS immersed in NaCl solution are presented as a function of different composition in Fig. 15. The capacitive arc radii of samples showed straight lines with high slope, which means double layer capacitor behavior of coating layers after 10 days of immersion. In consistence with Bode magnitude plot in Fig. 14(a), SS4 sample showed the highest impedance value along the ordinate which means excellent corrosion protection of tri-metal oxide nanocomposites for SS substrate. This result was also shown by Bode plot in Fig. 14, which can be ascribed to the perfect coating formation.

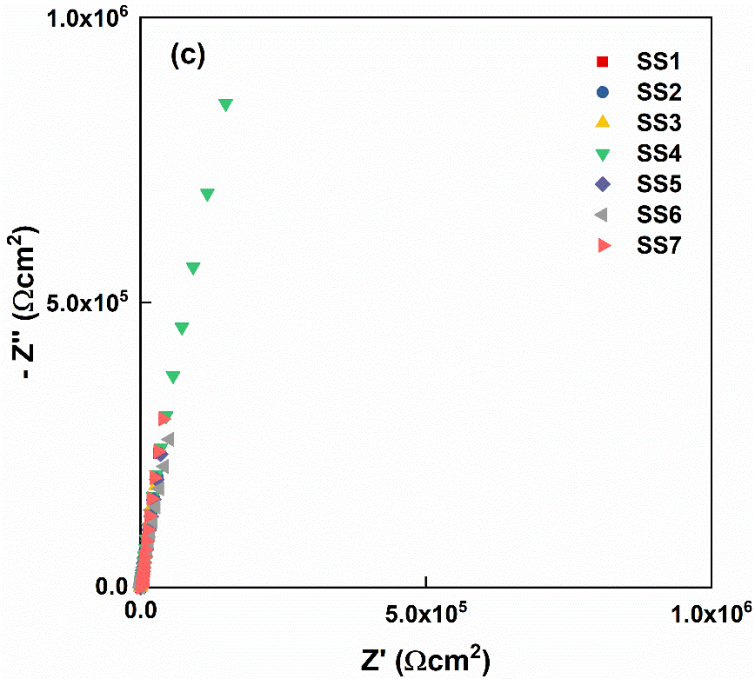

Figure 15. Nyquist plots of $ZrO_2/ZnO/TiO_2$ nanocomposites coated SS as a function of composition after 10 days immersed in NaCl solution.

3.2.5. Interpretation of impedance spectra by equivalent circuit models

To further obtain insight into the electrochemical process on bare metal substrates and ZrO_2/ZnO/TiO_2 coated metal substrate in 3.5% NaCl solution, the impedance results were analyzed with an equivalent circuit which involves the constant phase element (CPE) as shown by Fig. 16. The CPE model has commonly used for an equivalent description of a porous coating material, electric double layer, or heterogeneous coating material systems [54].

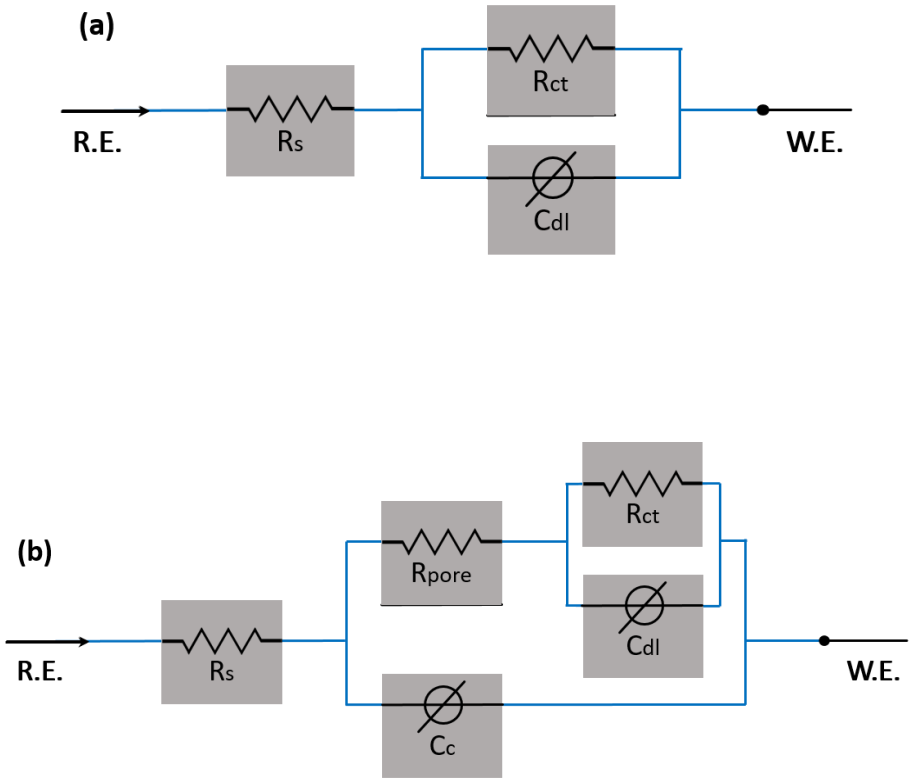

Figure 16. Equivalent circuit models used for the interpretation of the EIS results for carbon steel; (a) CPE and (b) damaged coating.

The fitting results based on the corresponding equivalent circuits are presented in Table 5. Three electrode potentiostat used in this study compensates for the solution resistance between the counter and reference electrodes. However, any solution resistance between the reference electrode and the working electrode must be considered. The EIS results are fitted with circuit models to calculate parameter including the solution resistance (R_s), charge transfer resistance (R_{ct}), double layer capacitance (C_{dl}), mass diffusion (W_d), coating resistance (R_{pore}), coating capacitance (C_c), respectively.

Table 5. Impedance parameters for bare and ZrO_2/ZnO/TiO_2 nanocomposites coated CS in NaCl solution after immersed for 10 days

Samples	R_s (Ω cm^2)	R_{ct} (Ω cm^2)	C_{dl} (F/cm^2)	R_{pore} (Ω cm^2)	C_c (F/cm^2)
CS1	2.87E+01	1.59E+03	7.76E-04	-	-
CS2	2.93E+01	7.16E+03	5.46E-04	4.18E+02	3.81E-04
CS3	2.42E-01	7.16E+03	1.54E-03	9.40E+01	1.20E-05
CS4	1.00E+02	4.68E+03	1.33E-03	5.92E+00	8.03E-05
CS5	2.50E+01	1.01E+03	2.12E-04	7.82E+02	4.63E-04
CS6	2.60E+01	1.82E+03	4.23E-04	1.57E+02	4.55E-04

From corresponding equivalent circuits are presented in Fig. 16 (a) and (b), double layer capacitance value of nanocomposite coated CS3 can be found to be C_{dl} ~5.46E-04 F/cm^2 lower than uncoated CS1 (C_{dl} ~7.76E-04 F/cm^2). It is natural that uncoated CS1 has a poor corrosion protection behavior. The lower resistance explains the obstruction of

charge accumulation at CS/NaCl solution by nanocomposite coating. As a result, the coated CS exhibits higher corrosion resistance about 3.81E-04 Ωcm^2 under nanocomposite coating, which implies an efficient blocking of the passage of ions from the NaCl solution to CS surface. The fitting results showed the increase of coating resistance and decrease of coating capacitance, which indicates that the corrosion protection performance of the nanocomposite coating has been improved. The increase of the corrosion protection performance is due to lack of local micro-cracks formed on the nanocomposite coating surface as shown in Fig. 11.

To obtain process on bare SS and ZrO_2/ZnO/TiO_2 coated SS substrates in 3.5% NaCl solution, the impedance results were analyzed with an equivalent circuit which involves the CPE model as shown by Fig. 17. The fitting results based on the corresponding equivalent circuits are presented in Table 6.

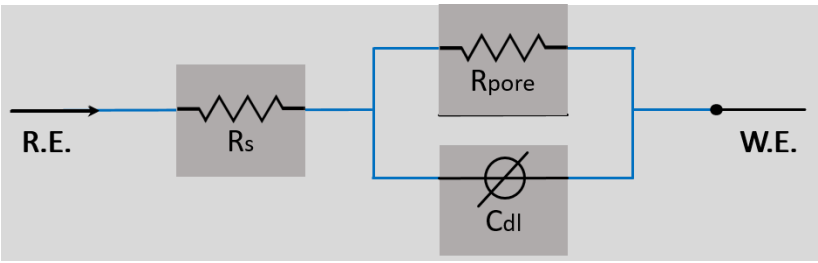

Figure 17. Equivalent circuit model used for the interpretation of the EIS results for stainless steel.

Table 6. Impedance parameters for bare and $ZrO_2/ZnO/TiO_2$ nanocomposites coated SS in NaCl solution after immersed for 10 days

Samples	R_s (Ω cm^2)	R_{ct} (Ω cm^2)	C_{dl} (F/cm^2)	α
SS1	3.91E+01	3.49E+11	1.93E-05	0.86
SS2	3.63E+01	9.15E+10	2.37E-05	0.87
SS3	8.12E+01	1.83E+11	2.46E-05	0.91
SS4	2.80E+02	1.24E+07	5.06E-06	0.93
SS5	4.93E+01	9.03E+10	1.94E-05	0.87
SS6	4.52E+01	1.30E+11	1.66E-05	0.84
SS7	3.44E+01	1.70E+11	1.55E-05	0.91

C_{dl} of SS4 showed one order (5.06E-06 F/cm^2) lower values than that of bare sample SS1 (1.93E-05 F/cm^2). This lower admittance values are attributed to a higher capacity to accumulate charges at SS substrate/NaCl solution interface by nanocomposite coating. Comparing α value (0.86) of bare sample SS1, one of nanocomposite coated SS4 (0.93) exhibited close to "1" which means which means that the nanocomposite layer shows a behavior close to a perfect capacitor. The fitting results show the increase of coating resistance and decrease of coating capacitance, which indicates that the corrosion protection performance of the nanocomposite coating has been improved. The increase of the corrosion protection performance is due to lack of local micro-cracks formed on the nanocomposite coating surface from SEM and mapping results as shown in Figs. 10 and 11.

4. CONCLUSIONS

We have synthesized the powder sample of trimetallic oxide nanocomposites based on zirconium (Zr), zinc (Zn), and titanium (Ti) by mechanochemical process as a function of milling time (3 hr to 17 hr). Furthermore, synthesis of powder sample varying the composition of trimetallic oxide nanocomposites of ZrO_2/ZnO/TiO_2; 90/5/5, 80/10/10, 65/10/25, 50/10/40, 40/10/50, and 10/80/10 keeping the constant milling time (3 hr) was done. Basic characterizations including XRD, Raman, SEM, EDS was performed to the synthesized powder samples. Metallization of the milled powder having the polycrystalline nature was observed from the XRD pattern. The individual phase was identified for the powder sample milled for lower milling time. The sample milled for 17 hr showed the better crystallinity with a formation of orthorhombic crystal structure belonging to Ti/ZrO bimetallic phase along (311) reflection plane owing to the higher energy for the inter-diffusion. The crystalline nature of combined nanocomposites was observed for the sample with different compositions milled for 3 hr. The RF sputtered ultra-thin coatings using aforementioned six different compositions were characterized structurally, morphologically, and electrochemically. Raman spectroscopy revealed the crystalline nature of sputtered films with the existence of A_g and B_g broad band Raman spectra. Compactly arranged grains were distributed to all the films with the little variance of grain size ranged from 22 nm to 26 nm depending upon the composition of metal oxide. Chemical compositions of the sputtered films were investigated by EDS coupled with SEM.

The coating was made on CS and SS with a target prepared from four different compositions via radio frequency sputtering to investigate the performance of coatings studied by EIS. From the Bode plots, the impedance of ZrO_2-rich composition coated CS and SS samples exhibited higher values about 3 - 4 times of magnitude than those of bare samples at the low frequency region after 10 day immersion. Phase angle values of ZrO_2-rich composition coated CS and SS samples showed around -48° and -82°, respectively. Relatively denser pore structure with uniform distribution morphologies of ZrO_2/ZnO/TiO_2 nanocomposites makes it more difficult for NaCl solution to penetrate into coating layer on CS and SS substrates. ZrO_2 seems to inhibit the corrosion more strongly on the interface between NaCl solution and coating layers. ZrO_2 would facilitate to good corrosion protection of CS and SS coated by ZrO_2/ZnO/TiO_2 nanocomposites.

REFERENCES

1. F. Sanchez, K. Sobolev, Constr. Build. Mater. 24, 2060 (2010)
2. K.E. Drexler, Bull. Sci. Technol. Soc. 24, 21 (2004)
3. G. Sharma, D. Kumar D, A. Kumar, H. Ala'a, D. Pathania, M. Naushad, G.T. Mola, Mater. Sci. Eng., C 71, 1216 (2017)
4. H. Bönnemann, R.M. Richards, Eur. J. Inorg. Chem. 10, 2455(2001)
5. P. Venkatesan and J. Santhanalakshmi, J. Mol. Catal. A: Chem. 326, 99 (2010)
6. Y. Tan, X. Dai, Y. Li, D. Zhu. J. Mater. Chem. 13, 1069 (2003)
7. S. Hasan, Res. J. Recent. Sci. 4, 1 (2015)
8. R.H. Baughman, A.A. Zakhidov, W.A. De Heer, Science 297, 787 (2002)
9. G. Dresselhaus, S. Riichiro, Physical Properties of Carbon Nanotubes, 1st edn. (Imperial College Press, 1998), pp. 49-72.
10. Z. Nie, A. Petukhova, E. Kumacheva, Nat. Nanotechnol. 5, 15 (2010)
11. D.E. Owens III, N.A. Peppas, Int. J. Pharm. 307, 93 (2006)
12. W. Li, F.C. Szoka, Pharm. Res. 24, 438 (2007)
13. J. Homola, S.S. Yee, G. Gauglitz, Sens. Actuators, B 54, 3 (1999)
14. Y. Ding, M. Chen, J. Erlebacher, J. Am. Chem. Soc. 126, 6876 (2004)
15. B. Singh, L. Murad, F. Laffir, C. Dickinson, E. Dempsey, Nanoscale 3, 3334(2011)
16. G. Sharma, M. Naushad, A. Kumar, S. Devi, M.R. Khan, Iran. Polym. J. 24, 1003 (2015)
17. J. Bian, M. Xiao, S. Wang, X. Wang, Y. Lu, Y. Meng, Chem. Eng. J. 147, 287 (2009)
18. B.Karthikeyan, B Loganathan, Mater. Lett. 85, 53 (2012)

19. G. Sharma, S. Bhogal, M. Naushad, A. Kumar, F.J. Stadler, J. Photochem. Photobiol., A 347, 235(2017)
20. M.A. Subhan, T. Ahmed, P. Sarker, T.T. Pakkanen, M. Suvanto, M. Horimoto, H. Nakata, J. Lumin. 148, 98 (2014)
21. K. Ding, Y. Li, Y. Zhao, J. Zhao, Y. Chen, Q. Wang, Int. J. Electrochem. Sci. 10, 8844 (2015)
22. V. Raghuveer, P.J. Ferreira, A. Manthiram, Electrochem. Commun. 8, 807 (2006)
23. J.L. Rupp, B. Scherrer, L.J. Gauckler, Phys. Chem. Chem. Phys. 12, 11114 (2010)
24. E.W. Van Stryland, H. Vanherzeele, M.A. Woodall, M.J. Soileau, A.L. Smirl, S. Guha, T.F. Boggess, Opt. Eng. 24, 244613 (1985)
25. K. Tanabe, T. Yamaguchi, Catal. Today 20, 185 (1994)
26. C. Yuan, H.B. Wu, Y. Xie, X. W. Lou, Angew. Chem. Int. Ed. 53, 1488 (2014)
27. M.A. Malik, M.A. Hashim, F. Nabi, S.A. Al-Thabaiti, Z. Khan, Int. J. Electrochem. Sci. 6, 1927 (2011)
28. P.F. Manicone, P.R. Iommetti, L. Raffaelli, Int. J. Dent. 35, 819 (2007)
29. S.M. Ho, J. Mater. Sci. Eng. 54, 23 (1982)
30. G. Teufer, Acta Crystallogr. 15, 1187 (1962)
31. K.S. Mazdiyasni, C.T. Lynch, J.S. Smith, J. Am. Ceram. Soc. 49, 286 (1966)
32. M. Li, Z. Feng, G. Xiong, P. Ying, Q. Xin, C. Li, J. Phys. Chem. B 105, 8107(2001)
33. R.C. Garvie, J. Phys. Chem. 82, 218 (1978)
34. M. Yoshimura, Am. Ceram. Soc. Bull. 67, 1950 (1988)
35. A. Fujishima, T.N. Rao, D.A. Tryk, J. Photochem. Photobiol. C. 1, 1 (2000)

36. M. Pelaez, N.T. Nolan, S.C. Pillai, M.K. Seery, P. Falaras, A.G. Kontos, M.H. Entezari, Appl. Catal., B 125, 331 (2012)
37. R.I. Bickley, T. Gonzalez-Carreno, J.S. Lees, L. Palmisano, R.J. Tilley. J. Solid State Chem. 92, 178 (1991)
38. G.H. Du, Q. Chen, R.C. Che, Z.Y. Yuan, L.M. Peng, Appl. Phys. Lett. 79, 3702 (2001)
39. X. Chen, S.S. Mao, Chem. Rev. 107, 2891 (2007).
40. M. Pelaez, N.T. Nolan, S.C. Pillai, M.K. Seery, P. Falaras, A.G. Kontos, M.H. Entezari, Appl. Catal. B. 125, 331 (2012)
41. D. Lenz, M. Delamar, C.A. Ferreira, J. Electroanal. Chem. 540, 35 (2003)
42. Z.L. Wang, J. Phys.: Condens. Matter. 16, R829 (2004).
43. C. Jagadish, S.J. Pearton, Zinc oxide bulk, thin films and nanostructures: processing, properties, and applications, 1st edn. (Elsevier, 2006) pp. 1-21.
44. G. Regmi, M. Rohini, P. Reyes-Figueroa, A. Maldonado, M. de la Luz Olvera, S. Velumani, J. Mater. Sci.- Mater. Electron 29, 15682 (2018)
45. C.B. Ong, L.Y. Ng, A.W. Mohammad, Renewable and Sustainable Energy Rev. 81, 536 (2018)
46. P. Vishnukumar, S. Vivekanandhan, M. Misra, A.K. Mohanty, Mater. Sci. Semicond. Process. 80, 143 (2018).
47. D.E. Talbot, J.D. Talbot, Corrosion science and technology, 3rd edn. (CRC press, 2018) pp.1-12.
48. P.F. Manicone, P.R. Iommetti, L. Raffaelli, J. Dent. 35, 819 (2007)
49. Y. Lan, Y. Lu, Z. Ren, Nano Energy 2, 1031 (2013)
50. NF. Hamedani, F. Farzaneh, J. Sci. I.R.I. 17, 231 (2006)

51. R.C. Garvie, J. Phys. Chem. 69, 1238 (1965)

52. P. Laffez, P. Daniel, A. Jouanneaux, N.T. Khoi, D. Siméone, Mater. Sci. Eng., B. 104 (3), 163 (2003)

53. R. Wang, X. He, Y. Gao, X. Zhang, X. Yao, B. Tang, Mater. Sci. Eng., C. 75, 7 (2017)

54. S. Cho, T. Chiu, H. Castaneda, Electrochim. Acta 316, 189 (2019)